Variational Deformation Method for the Computation of the Average Shape of Organs

Shun Inagaki
School of Advanced Integrate Sciences
Chiba University
Yayoi-cho 1-33, Inage-ku
Chiba 263-8522, Japan

Atsushi Imiya
Inst. of Management and Information Technologies
Chiba University
Yayoi-cho 1-33, Inage-ku
Chiba 263-8522, Japan

Abstract

Multiple image warping computes deformation fields between an image and a collection of images. Using multiple warping, we develop a variational method for the computation of average images of volumetric biological organs. In medical diagnosis, the average shape of individual organs provides essential properties for the general expression of organs. For the comparative reading of medical images, image registration to a standard organ in database is achieved to discriminate abnormal organs from the standard organ. Our algorithm numerically generates a standard organ from a collection of volumetric medical images. Appling the multiple warping to the temporal sequence of a beating heart, we obtain the average heart.

1. Introduction

In this paper, we deal with multiple image warping, which computes deformation fields between an image and a collection of images. This collection of multiple deformation fields provides the average image and shape of a collection of volumetric images and objects. For a collection of spatiotemporal volumetric images, we can define the temporal average a sequence, the spatial average of the temporal average and temporal average of spatial average. We clarify relations among these three averages of Appling the temporal average computation to sequence of a beating heart, we obtain the average heart.

In medical diagnosis, the average shape of individual organs provides essential properties for the general expression of organs [1]. In computational anatomy, the statistical average shape, which is computed using principal component analysis of a shape descriptor, is well defined [2]. In both structure pattern recognition [3, 4] and variational registration [1], the average shape among a collection of given shapes is of interest. There are various methods for computing the average shape [5, 6]. These methods are based on the mathematical definition that shapes are the boundary contours of physical objects with shapes defined in the shape space [7]. This definition is suitable for dealing with highly nonlinear geometric variations.

Furthermore, in comparative reading of medical images, image registration is the main method used to classify the differences among the images. In particular, the establishment of local deformations between a collection of given shapes has attracted researchers of medical image analysis for decades. Some pioneering works demonstrated a registration process achieved by pattern matching based on dynamic programming [8, 9], which is a fundamental idea in pattern recognition. These approaches involve the matching and retrieval of occluded shapes, and they are intended for the global alignment of planar shapes. The shape-matching algorithm observes a collection of given shapes, detects the contours and then computes (1) distances among them and (2) point correspondences between the contours [10]. However, it tends to be less accurate in the representation of local structures because the point correspondences are computed without preserving the geometric local structure of the shapes. In structure pattern recognition [3, 4] the average of a collection of combinatorial structures such as strings and graphs is of interest.

Warping and morphing are fundamental techniques in computer graphics to interpolate and generate shapes and objects. In medical applications, morphing is used for the description of the deformation process of biological organs. This process predicts the deformable motion of biological organs in the human torso such as the beating heart and the deformation of the lungs during breathing. In medical image diagnosis and retrieval [11, 12], average images and shapes of individual organs provide essential properties for the general expression of organs. Shape retrieval cat-

egorises and classifies shapes, and finds shapes from portions of shapes. In shape retrieval, the matching of shapes is based on the diffeomorphism of shapes [13, 14] and the descriptor of shape boundary contours [10, 8] are used. In the matching process for discrete shapes, the string edit distance [3, 4] computed by dynamic programming is a fundamental tool. Moreover, in the matching process of images, the variational registration strategy [11, 12] is a typical tool.

2. Variational Average Computation

Multiple Warping

For a function $f(\boldsymbol{x})$ defined on a finite region Ω in the n-dimensional Euclidean space $\mathbf{R}^n$ and a transform $\phi(\boldsymbol{x})$ from $\mathbf{R}^n$ to $\mathbf{R}^n$, the transform $\phi \circ f = f(\phi(\boldsymbol{x}))$ is called the morphing of f by ϕ. Setting ϕ_k to an appropriate deformation operation applied to each f_k for $k = 1, 2, \cdots, m$, we deal with the minimiser

$$J(\{\phi_k\}_{i=1}^n, g) = \sum_{i=1}^{m} \{d(f_k, \phi_k \circ g) + \mu P(\phi_k)\} + \lambda Q(g), \tag{1}$$

which simultaneously computes g and ϕ_k for an appropriate metric $d(f, g)$ over a collection of images, where P and Q are the regularisers for ϕ_k and g, respectively.

We call the minimization problem defined by eq. (1) multiple warping from $\{f_k\}_{k=1}^m$ to g. From multiple warping, we define the temporal average a sequence, the spatial average of the temporal average and temporal average of spatial average. We clarify relations among these three averages of Appling the temporal average computation to sequence of a beating heart, we obtain the average heart.

Setting the data size of a volumetric image to be $N = G \cdot H \cdot V \cdot D$, where G, H, V and D are the number of levels of grey values, the horizontal resolution, the vertical resolution and the depth resolution, respectively, the total numbers of data for static and temporal volumetric-image multiple warping are $T_s = N \times m$ and $T_t = N \times m \times p$, respectively, where m and p are the numbers of images and phase in a sequence, respectively. Therefore, data size of multiple warping for the variational average computation is relatively large comparing to traditional image registration.

Group Average

For volumetric images $\{f_i(\boldsymbol{x})\}_{i=1}^m$ for $\boldsymbol{x} \in \mathbf{R}^n$ we define the variational average g as the minimiser of the variational problem

$$\begin{aligned} J_G &= \sum_{k=1}^{m} \int_{\mathbf{R}^3} g(\boldsymbol{x} - \boldsymbol{u}_k) - f_k(\boldsymbol{x}))^2 d\boldsymbol{x} \\ &\quad + \mu \sum_{k=1}^{m} \int_{\mathbf{R}^3} |\nabla \boldsymbol{u}_k|^2 d\boldsymbol{x} + \sigma \int_{\mathbf{R}^3} \left(\sum_{k=1}^{m} \boldsymbol{u}_k \right)^2 d\boldsymbol{x} \\ &\quad + \lambda \int_{\mathbf{R}^3} |\nabla g|^2 d\boldsymbol{x}, \end{aligned} \tag{2}$$

where

$$\Gamma = \int_{\mathbf{R}^3} |\nabla g|^2 d\boldsymbol{x},\ U_k = \int_{\mathbf{R}^3} |\nabla \boldsymbol{u}_k|^2 d\boldsymbol{x},\ S = \sum_{k=1}^{m} \boldsymbol{u}_k, \tag{3}$$

are regularisers for g and deformation fields $\{\boldsymbol{u}_k\}_{k=1}^n$. The constraints Γ and U_k imply that the average g and the deformation field are smooth, respectively. The constraint S implies that the average image exists at the median point of the deformation field. We set the minimiser of eq. (2) f_G and call f_G the group average.

Temporal Average

The temporal average $g(t)$ for $0 \le t \le T$ of $\{f_i(t), 0 \le t \le T_i\}_{i=1}^m$ is the minimiser of

$$J_2 = \int_0^T \{\sum_{k=1}^{m} (f_k(t) - g(\phi_k(t)))^2 + \lambda_i P(\phi_k(t)) + \kappa R(g)\} dt, \tag{4}$$

where P and R are regularisers and ϕ_k is a function from $[0, T_i]$ to $[0, T]$. We extend the this procedure to the spatiotemporal data $f(\boldsymbol{x}, t)$ $0 \le t \le T$.

The temporal average g of $f(\boldsymbol{x}, t)$ $0 \le t \le T$, is the minimiser of the functional

$$\begin{aligned} J_T &= \int_{\mathbf{R}^3} \int_0^T (f(\boldsymbol{x}, t) - g(\phi(\boldsymbol{x}, t)))^2 \\ &\quad + \lambda P(\phi(\boldsymbol{x}, t)) + \kappa R(g)\} dt d\boldsymbol{x} \end{aligned} \tag{5}$$

We set the minimiser of eq.(5) to be f_T. If

$$P(\phi(\boldsymbol{x}, t)) = |\nabla \phi|^2 + |\partial_t \phi|^2, \tag{6}$$

$$R(g) = |\nabla g|^2 = |\nabla g|^2 + |\partial_t g|, \tag{7}$$

we have the Euler-Lagrange equations

$$-(f(\boldsymbol{x}, t) - g(\phi(\boldsymbol{x}, t)))\boldsymbol{J}_\phi \nabla_t g - \lambda_i \Delta_t \phi = 0 \tag{8}$$

$$-\int_0^T (f(\boldsymbol{x}, t) - g(\phi(\boldsymbol{x}, t)))dt - \lambda \Delta g = 0 \tag{9}$$

where $\nabla_t = (\nabla^\top, \partial_t)^\top$ and $\Delta_t = \Delta + \partial_t^2$ are spatiotemporal operations and $\boldsymbol{J}_f$ is the Jacobian of f.

Furthermore, if we set $\phi(\boldsymbol{x},t)=\boldsymbol{x}+\boldsymbol{u}(t)$, we have the criterion

$$J_{T2} = \int_{\mathbf{R}^3}\int_0^T (f(\boldsymbol{x},t)-g(\boldsymbol{x}+\boldsymbol{u}(t)))^2 dtd\boldsymbol{x} + \int_{\mathbf{R}^3}\int_0^T \lambda P(\boldsymbol{u}(t))+\kappa R(g)\}dtd\boldsymbol{x}. \quad (10)$$

Moreover, if the sequence of samples $\{f(\boldsymbol{x},\delta k)\}_{k=0}^{m-1}$ for a fixed δ such that $\delta m = T$ is measured, we have the temporally discrete criterion

$$J_{T3} = \int_{\mathbf{R}^3}\sum_{k=0}^{m-1} (f(\boldsymbol{x},\delta k)-g(\boldsymbol{x}+\boldsymbol{u}_k))^2 d\boldsymbol{x} + \int_{\mathbf{R}^3}\sum_{k=0}^{m-1} \lambda P(\boldsymbol{u}_k)+\kappa R(g)\}d\boldsymbol{x}. \quad (11)$$

Group Temporal Average

Setting $f_i(\boldsymbol{x})$ to be the temporal average of $\{f_i(\boldsymbol{x},t)\}_{i=1}^m$, the group temporal average of $f_i(\boldsymbol{x},t)$ defined on $\mathbf{R}^3\times[0,T_i]$ is the minimiser of the functional

$$J_{GT} = \int_{\mathbf{R}^3}\{\sum_{i=1}^m (f_i(\boldsymbol{x})-g(\psi_i(\boldsymbol{x})))^2+\lambda_i P(\psi_i(\boldsymbol{x}))+\kappa R(g)\}\boldsymbol{x}. \quad (12)$$

If we set $\psi_i(\boldsymbol{x})=\boldsymbol{x}+\boldsymbol{u}_i$, we have the criterion

$$J_{TG2} = \int_{\mathbf{R}^3}\{\sum_{i=1}^m (f_i(\boldsymbol{x})-g(\boldsymbol{x}+\boldsymbol{u}_i)^2+\lambda_i P(\boldsymbol{u}_i)+\kappa R(g)\}\boldsymbol{x}. \quad (13)$$

Temporal Group Average

For a collection of temporal volumetric images $f_i(\boldsymbol{x},t)$, if we set $f_i(\boldsymbol{x}) := f_i(\boldsymbol{x},T)$, the spatial average at time $t=T$ is the minimiser of

$$J_{TG} = \sum_{k=1}^m \int_{\mathbf{R}^3} g(\boldsymbol{x}+\boldsymbol{u}_k)-f_k(\boldsymbol{x}))^2 d\boldsymbol{x} + \mu\sum_{k=1}^m\int_{\mathbf{R}^3}|\nabla\boldsymbol{u}_k|^2 d\boldsymbol{x}+\sigma\int_{\mathbf{R}^3}\left(\sum_{k=1}^m \boldsymbol{u}_k\right)^2 d\boldsymbol{x} + \lambda\int_{\mathbf{R}^3}|\nabla|^2 d\boldsymbol{x}. \quad (14)$$

For these four averages of spatio-temporal volumetric images, we have the following property.

Property 1 *Setting* $f_{TG} = arg(\min J_{TG})$ *and* $f_{GT} = arg(\min J_{GT})$, *the relation* $f_{GT}\neq f_{TG}$ *is satisfied.*

Figure 1 shows methods for the computation of the volumetric average-shape of three-dimensional organs. Although the average shape of usual organs is computed by the one step method, the average shape of temporal organs, such as beating hearts, is computed by the bi-step method. First, we compute the temporal average shape of an organ. Then, the spatial average is computed from individual temporal averages.

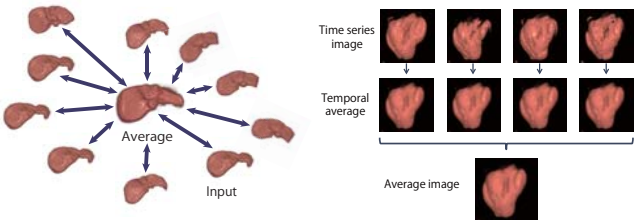

(a) Spatial average (b) Temoral average

Figure 1. Average image. (a) The average shape of usual organs is computed by the uni-step method. (b) The average shape of temporal organs, such as beating hearts, is computed by the bi-step method. The first, we compute the temporal average of an organ. Then, the spatial average is computed from individual temporal averages.

3. Numerical Method

The Euler-Lagrange equations for the computation of f_* for $*\in\{T,G,TG,GT\}$ are in the same class of the partial differential equations. Therefore, we derive a numerical method for eq. (2).

From eq. (2), for the variational average image g and deformation fields $\boldsymbol{u}_k$ we derive the Euler-Lagrange equations,

$$\alpha\Delta g(\boldsymbol{x})-G=0,\quad \beta\Delta\boldsymbol{u}_k(\boldsymbol{x})-U_k=0, \quad (15)$$

where

$$G = \sum_{k=1}^m (g(\boldsymbol{x})-f_k(\boldsymbol{x}-\boldsymbol{u}_k)), \quad (16)$$

$$U_k = \gamma(\sum_{k=1}^m \boldsymbol{u}_k+(g(\boldsymbol{x})-f_k(\boldsymbol{x}-\boldsymbol{u}_k)) \times\nabla(g(\boldsymbol{x})-f_k(\boldsymbol{x}-\boldsymbol{u}_k))). \quad (17)$$

Next, we convert eq. (15) to the diffusion equations

$$\frac{\partial g}{\partial t}=\Delta g(\boldsymbol{x})-\frac{1}{\alpha}G,\quad \frac{\partial\boldsymbol{u}_k}{\partial t}=\Delta\boldsymbol{u}_k(\boldsymbol{x})-\frac{1}{\beta}U_k, \quad (18)$$

and discretise them as

$$\frac{g^{(n+1)} - g^{(n)}}{\tau} = \boldsymbol{L} g^{(n+1)} - \frac{1}{\alpha} G^{(n)}, \quad (19)$$

$$\frac{\boldsymbol{u}_k^{(n+1)} - \boldsymbol{u}_k^{(n)}}{\tau} = \boldsymbol{L} \boldsymbol{u}_k^{(n+1)} - \frac{1}{\beta} U_k^{(n)}, \quad (20)$$

where $\boldsymbol{L}$ is the discrete Laplacian operation. Therefore, we obtain the iteration forms [17]

$$(\boldsymbol{I} - \tau \boldsymbol{L}) g^{(n+1)} = g^{(n)} - \frac{\tau}{\alpha} G^{(n)}, \quad (21)$$

$$(\boldsymbol{I} - \tau \boldsymbol{L}) \boldsymbol{u}_k^{(n+1)} = \boldsymbol{u}_k^{(n)} - \frac{\tau}{\beta} U_k^{(n)}. \quad (22)$$

In each step of the iteration, the results are expressed on the Euler frame. Image sampled by the Lagrange frame do not guarantee correspondence between points. Therefore, we resample the results using the Lagrange frame [1]. In the Lagrange-frame-sampled images, we use Delaunay-triangle-based interpolation [18] since the method satisfies the minimum gradient property.

The iteration forms [17] derived in the previous sections are described in the form

$$(\boldsymbol{I} - \tau \boldsymbol{L}) \boldsymbol{a}^{(n+1)} = \boldsymbol{a}^{(n)} - f(\boldsymbol{a}^{(n)}). \quad (23)$$

where $\boldsymbol{L}$ is the discrete Laplacian matrix. For three-dimensional problems, $\boldsymbol{L}$ are described as

$$\boldsymbol{L} = \boldsymbol{D} \otimes \boldsymbol{I} \otimes \boldsymbol{I} + \boldsymbol{I} \otimes \boldsymbol{D} \otimes \boldsymbol{I} + \boldsymbol{I} \otimes \boldsymbol{I} \otimes \boldsymbol{D}, \quad (24)$$

for

$$\boldsymbol{D} = \begin{pmatrix} -1 & 1 & 0 & \cdots & 0 & 0 & 0 \\ 1 & -2 & 1 & \cdots & 0 & 0 & 0 \\ 0 & 1 & -2 & \cdots & 0 & 0 & 0 \\ \vdots & \vdots & \vdots & \ddots & \vdots & \vdots & \vdots \\ 0 & 0 & 0 & \cdots & 1 & -2 & 1 \\ 0 & 0 & 0 & \cdots & 0 & 1 & -1 \end{pmatrix}, \quad (25)$$

where $\boldsymbol{A} \otimes \boldsymbol{B}$ is the Kronecker product of matrices $\boldsymbol{A}$ and $\boldsymbol{B}$, assuming the von-Neumann condition on the boundary.

The eigenvalues of $\boldsymbol{D}$ are $\lambda_k = 4 \sin^2 \frac{\pi k}{2M}$ for the $M \times M$ matrix [15], and the eigenmatrix [16] of $\boldsymbol{D}$, is

$$\boldsymbol{\Phi} = \left(\left(\epsilon \cos \frac{(2j+1)i}{2\pi} \pi M \right) \right), \ \epsilon = \begin{cases} 1 & \text{if } j = 0 \\ \frac{1}{\sqrt{2}} & \text{otherwise.} \end{cases} \quad (26)$$

$\boldsymbol{\Phi}$ is the matrix of the DCT-II transform. Therefore, the matrix $\boldsymbol{L}$ is decomposed as

$$\begin{aligned} \boldsymbol{L} &= (\boldsymbol{\Phi} \otimes \boldsymbol{\Phi} \otimes \boldsymbol{\Phi}) \\ &\quad \times (\boldsymbol{\Lambda} \otimes \boldsymbol{I} \otimes \boldsymbol{I} + \boldsymbol{I} \otimes \boldsymbol{\Lambda} \otimes \boldsymbol{I} + \boldsymbol{I} \otimes \boldsymbol{I} \otimes \boldsymbol{\Lambda}) \\ &\quad \times (\boldsymbol{\Phi} \otimes \boldsymbol{\Phi} \otimes \boldsymbol{\Phi})^\top \\ &= \boldsymbol{U} \boldsymbol{\Sigma} \boldsymbol{U}^\top \end{aligned} \quad (27)$$

[1] There are two reference frames, which are called the Euler frame and Lagrange frame [12]. When we have an image B and an invertible transform φ, the frames are described as $B^{Lagrange}(\varphi(i,j)) := B(i,j)$ and $B^{Euler}(i,j) := B(\varphi^{-1}(i,j))$.

Table 1. Parameters for computation

		α	β	γ
Liver,	Female	10^{-1}	10^2	10^3
	Male	10^{-1}	10^2	10^3
	Mixed	10^{-1}	10^2	10^3
Heart		10^{-1}	10^3	10^4

and the eigenvalues of $\boldsymbol{L}$ are $\lambda_i + \lambda_j + \lambda_k$. Then, since eq. (23) is redescribed as

$$\boldsymbol{U} \boldsymbol{\Sigma} \boldsymbol{U}^\top \boldsymbol{a}^{(n+1)} = \boldsymbol{a}^{(n)} - f(\boldsymbol{a}^{(n)}), \quad (28)$$

we have the iteration form

$$\boldsymbol{a}^{(n+1)} = \boldsymbol{U}^\top (\boldsymbol{I} - \tau \boldsymbol{\Sigma})^{-1} \boldsymbol{U} (\boldsymbol{a}^{(n)} - f(\boldsymbol{a}^{(n)})), \quad (29)$$

where

$$(\boldsymbol{I} - \tau \boldsymbol{\Sigma})^{-1} = Diag \left(\frac{1}{1 - \tau(\lambda_i + \lambda_j + \lambda_k)} \right), \quad (30)$$

that is, $\boldsymbol{a}^{(n+1)}$ is numerically computed from $\boldsymbol{a}^{(n)}$ using DC(S)T-II [16] and a filtering operation for the Neumann boundary condition.

4. Numerical Examples

We show computational results for the first, second and third averages. For the first average, we have computed the average of 7 female livers and 25 male livers. For the second and third average, we computed the temporal averages of 7 beating hearts.

We evaluate the warp image error WIE, the total deformation norm FNS, the volume V_i and the deformation energy DE_k which are defined as

$$\begin{aligned} \mathrm{WIE}(\boldsymbol{x}) &= \int_{\mathbf{R}^3} \|g(\boldsymbol{x}) - f_i(\boldsymbol{x} - \boldsymbol{u}_k)\|_2 d\boldsymbol{x}, \\ \mathrm{FNS}(\boldsymbol{x}) &= \| \sum_{i=1}^{n} \boldsymbol{u}_i \|_2, \\ V_k &= \int_{\mathbf{R}^3} f_k(\boldsymbol{x} - \boldsymbol{u}_k) d\boldsymbol{x}, \\ DE_k &= \int_{\mathbf{R}^3} ||\boldsymbol{u}_k(\boldsymbol{x})||_2^2 d\boldsymbol{x}. \end{aligned}$$

Furthermore, we show the relation between the input volumetric data and averages using the multidimensional scaling. For the numerical computation, we adopt the regularisation parameters in Table 1.

The resolutions of livers and hearts are listed in table 4

Figures 2 (a), (b) and (c) show the linear average, and the eigenorgan, [2] which is the linear combination of the first

[2] See Appendix A for the computation of the eigenorgan.

Table 2. Resolutions of livers and hearts

Organ	Grayvalue	Horisontal	Vertical	Depth
Liver 32 data	256	87	97	76
Heart 20 phase 7 data	256	128	128	15

four principal functions in the organ space and the variational average, respectively, of 32 livers. As shown in Fig. 2, the boundary of the variational average is clear and sharp, although the boundary of the eigenorgan is blurred. This blurring on the boundary is caused by the geometric divergence of the boundary of each principal organ.

Figure 3 shows the distribution of the volumes and the average deformation vectors for 32 livers. Figure 5 shows a graphic expression of the multidimensional scaling of 32 livers. For the definition of the distance between a pair of organs see Appendix B. This graphical expression shows that the variational average lies at a position close to the average with respect to the rotation invariant distance of the volumetric images.

Figure 4 show the compass charts of the deformation for (a) the linear average, (b) the eigenorgan and (c) the variational average. The arrows show the total difference between the average and each shape on the cycle. The configuration of allows is symmetric for the variational average. This geometric configuration coincides with the configuration of samples in the multidimensional scaling. These charts imply that the variational average is stable and robust against outer layers, although the eigenorgan is sensitive to outer layers.

Figure 6 shows 20 temporal volumetric images of a sequence of a beating heart. Figures 7 (a), (b) and (c) show the compass charts of beating cycle of a beating heart for the variational temporal average, temporal eigenorgan and the linear average with respct to time. Figures 7 (d), (e) and (f) show the spatial average of the temporal averages, the eigenorgan of the temporal averages and the linear average with respect to time, respectively. In the compass chart of the beating heart, 20 phases of a beating heart are shown on the circle and the arrow from the origin of the circle is the deformation energy to deform the temporal average, which is shown in the centre of the chart, to each volumetric image at each phase.

The arrows show the total difference between the average and each shape on the cycle. These charts show that the variational average is a stable shape with respect to the cyclic deformation because the deformations on the chart are symmetry. However, the eigenorgan of the beating heart is unstable against cyclic motion because the deformation on the chart is asymmetric.

Figures 7 (a), (b) and (c) show the spatial average of the temporal averages, the eigenorgan of the temporal averages and the linear average with respect to time, respectively. Figures 8(a) and (b) show the totl deformation norms and The warp image errors, respectively for three averages. Figures 9(a) and (b) show th he spatial average of the temporal averages of 7 beating hearts. and the eigenorgan of the temporal averages of 7 beating hearts. Figure 9(c) shows the graphical MDS of the variational average.

The boundary of the spatial average of the temporal averages is smooth, although that of the eigenorgan contains small vibrations. These results show the variational average of the variational temporal averages is suitable for the construction of the model of the stationary heart of a man.

(a) (b) (c)

Figure 2. Comparison of the numerical averages. (a) The linear average. (b) The eigenorgan. (c) The variational average.

5. Conclusions

We introduced multiple image warping as an extension of variational registration. We also introduced the deformation compass chart to evaluate the performance of the average computation.

The multiple image warping computes deformation fields between an image and a collection of images. We developed a variational method for the computation of the average images and shapes of biological organs in three-dimensional Euclidean space. We combine the diffusion registration technique and optical flow computation for the computation of spatial deformation field between the average image and input organs. We defined the average shape as the shape which minimises the total deformation field.

For temporal volumetric images, we develop variational method for the computation of the temporal average and the spatial average. The temporal average of a beating heart constructs a model heart of an individual. This model shape of sequence of temporal volumetric shape illustrated deformation of a beating heart at each phase. Furthermore, as a combination of the computations of the temporal average and the spatial average. we defined the temporal average of spatial averages and spatial average of temporal averages. We clarified that these method derive different results.

This research was supported by the “Computational

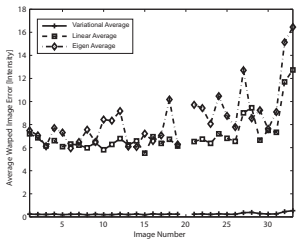

(a)

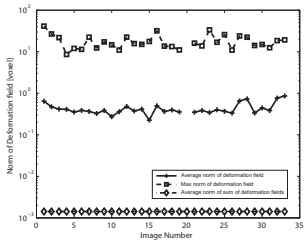

(b)

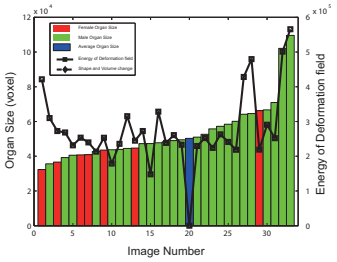

(c)

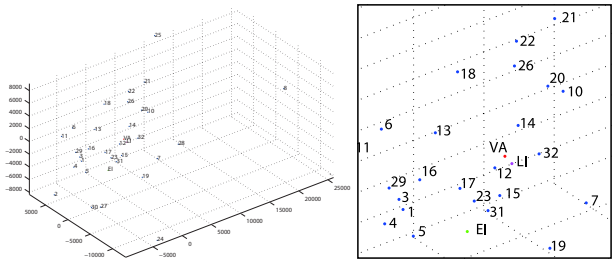

(d) (e)

Figure 3. Numerical evaluation (a) The warp errors of deformation. (b) The total deformation norms. (c) The deformation energies of livers (d) Graphical expression of the multi-dimensional scaling. (e) Magnification of the graphical MDS around the variational average.

anatomy for computer-aided diagnosis and therapy: Frontiers of medical image sciences" project funded by a Grant-in-Aid for Scientific Research on Innovative Areas from MEXT, Japan, and by Grants-in-Aid for Scientific Research funded by the Japan Society for the Promotion of Science.

Appendix

A. Eigenorgan

Since, for function $f(\boldsymbol{x})$ defined on $\mathbf{R}^3$,

$$f(x+\boldsymbol{\delta}) = f(\boldsymbol{x}) + \boldsymbol{\delta}^\top \nabla f$$

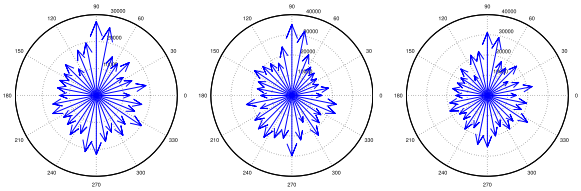

(a) Linear average (b) Eigenorgan (c) Variational average

Figure 4. Statistical analysis the averages of 32 livers. (a) Linear average. (b) Eugenorgan. (c) Variational average. Arrows from the center of the chart show the total deformation norm. The configuration of allows is symmetric for the variational average.

(a) Liver20 (b) Liver19

(c) Liver28 (d) Liver13

Figure 5. Examples of livers. (a) The variatioal average:20. (b) The liver of a male:19. (c) The liver of a male:28. (d) The liver of a female:13 The number labels of livers correspond to the number labels on the multidimensional scaling of Fig. 3 (d).

and

$$\int_{\mathbf{R}^3} f f_x d\boldsymbol{x} = 0, \quad \int_{\mathbf{R}^3} f_x f_y d\boldsymbol{x} = 0,$$
$$\int_{\mathbf{R}^3} f f_y d\boldsymbol{x} = 0, \quad \int_{\mathbf{R}^3} f_y f_z d\boldsymbol{x} = 0,$$
$$\int_{\mathbf{R}^3} f f_z d\boldsymbol{x} = 0, \quad \int_{\mathbf{R}^3} f_z f_x d\boldsymbol{x} = 0$$

in the neighbourhood of the point $\boldsymbol{x}$, the dimension of the image space is locally four. Therefore, using the local orthogonal base, the volumetric eigenimage is expressed as

$$f(\boldsymbol{x}) = \sum_{k=1}^{4} \alpha_k \boldsymbol{u}_k(\boldsymbol{x})$$

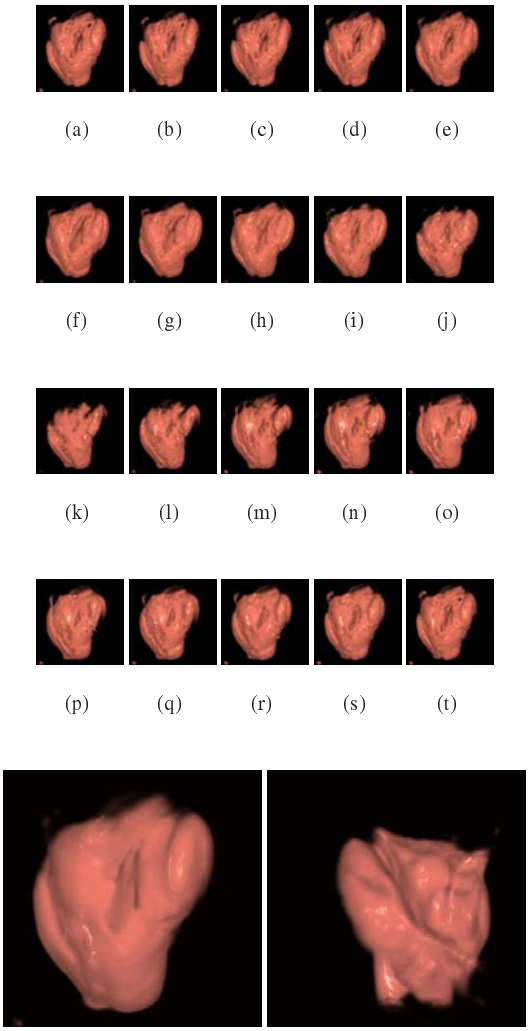

Figure 6. Sequence of volumetric beating-heart image and the temporal average shape. (a)-(t) are 20 input temporal image-sequence. (u) and (v) are two views of the temporal-average shape of the volumetric beating heart images.

where $\{\boldsymbol{u}_i\}_{i=1}^4$ are the first four principal components of the covariance kernel

$$K(\boldsymbol{x}, \boldsymbol{y}) = \sum_{i=1}^{n} f(\boldsymbol{x}) f(\boldsymbol{y}).$$

B. Volumetric Diatance

Setting

$$g_{\text{linear}}(\boldsymbol{x}) = \frac{1}{n} \sum_{i=1}^{n} f_i(\boldsymbol{x} - \boldsymbol{g}_i), \ \boldsymbol{g}_i = \frac{1}{\Omega} \int_{\mathbf{R}^3} f_i(\boldsymbol{x}) d\boldsymbol{x}$$

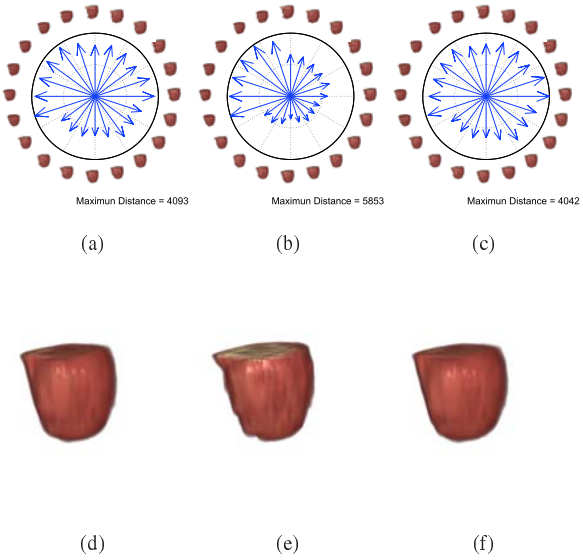

Figure 7. Comaprison of the three averages a beating heart. (a) The radar chart for the linear average a sequence of a beating heart. (b) The radar chart for the eigenorgan of a sequence of a beating heart. (c) The radar chart for the variational temporal average of a beating heart. (d) The linear average a sequence of a beating heart. (e) The eigenorgan of a sequence of a beating heart. (f) The variational average a sequence of a beating heart.

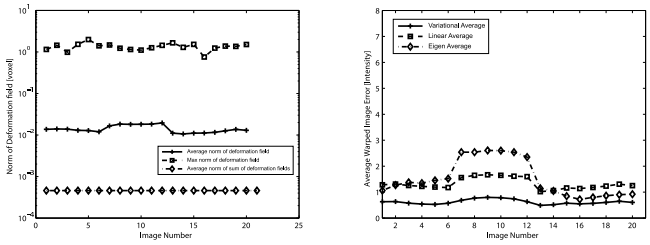

Figure 8. Comparison of the three averages a beating heart. (a) The total deformation norms (b) The warp errors

the volumetric distance is computed as

$$D(f, g) = \min_{\boldsymbol{R}} \int_{\mathbf{R}^3} |f(\boldsymbol{x}) - g(\boldsymbol{R}\boldsymbol{x})|^2 d\boldsymbol{x},$$

where the rotation $\boldsymbol{R}$ is computed by aligning landmarks.

References

[1] D.L.G. Hill, P.G. Batchelor, M. Holden, D.J. Hawkes, Medical image registration, Physics in Medicine and Biology, **46**, R1-45, 2001.

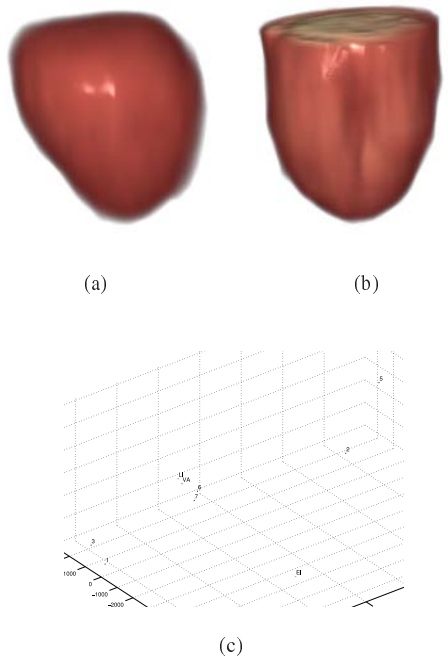

(a) (b)

(c)

Figure 9. Comparison of the averages a beating heart. (a) The spatial average of the temporal averages of 7 beating hearts. (b) The eigenorgan of the temporal averages of 7 beating hearts. (c) The graphical MDS of two types of variational averages.

[2] A. Srivastava, S. Joshi, W. Mio, X. Liu, Statistical shape analysis: Clustering, learning, and testing, IEEE PAMI, **27**, 590-602, 2005.

[3] T.B. Sebastian, P.N. Klein, B.B. Kimia, On aligning curves, IEEE PAMI, **25**, 116-125, 2003.

[4] K. Riesen, H. Bunke, Approximate graph edit distance computation by means of bipartite graph matching, IVC, **27**, 950-959, 2009.

[5] M. Rumpf, B. Wirth, A nonlinear elastic shape averaging approach, SIAM Imaging Science, **2**, 800-833, 2009.

[6] B. Avants, J.C. Gee, Geodesic estimation for large deformation anatomical shape averaging and interpolation, NeuroImage, **23**, S139–S150, 2004.

[7] M. Rumpf, B. Wirth, An elasticity-based covariance analysis of shapes, IJCV, **92**, 281-295, 2011.

[8] E. Milios, E. G. M. Petrakis, Shape retrieval based on dynamic programming, IEEE Image Processing, **9**, 141-147, 2000.

[9] C. Grigorescu, N. Petkov, Distance sets for shape filters and shape recognition, IEEE Image Processing, **12**, 1274-1286, 2003.

[10] E. M. Arkin, L. P. Chew, D. P. Huttenlocher, K. Kedem, J. S. B. Mitchell, An efficiently computable metric for comparing polygonal shapes, IEEE PAMI, **13**, 209-216, 1991

[11] B. Fischer, J. Modersitzki, Ill-posed medicine- an introduction to image registration, Inverse Problem., **24**, 1-17, 2008.

[12] J. Modersitzki, *Numerical Methods for Image Registration*, OUP, 2004.

[13] F. Arrate, J. T. Ratnanather, L. Younes, Diffeomorphic active contours. SIAM Imaging Science, **3**, 176-198, 2010.

[14] E. Sharon, D. Mumford, 2D-shape analysis using conformal mapping, IJCV, **70**, 55-75, 2006.

[15] J. W. Demmel, *Applied Numerical Linear Algebra*, SIAM, 1997.

[16] G. Strang, T. Nguyen, *Wavelets and Filter Banks*, Wellesley-Cambridge Press, 1996.

[17] R.S. Varga, *Matrix Iterative Analysis*:2nd Ed., Springer, 2000.

[18] Ø, Hjelle, M. Dæ hlen, *Triangulations and Applications, in Mathematics and Visualization Series*, Springer, 2006.